Journal of
Materials Chemistry A

Materials for energy and sustainability

Accepted Manuscript

This article can be cited before page numbers have been issued, to do this please use: D. G. Solanki, P. J. Sharma, S. A. Bhakhar, M. Nandpal, S. Patel, V. Chakkooth, S. Sharma, C. Sumesh and P. M. Pataniya, *J. Mater. Chem. A*, 2026, DOI: 10.1039/D6TA00999A.

ROYAL SOCIETY OF CHEMISTRY

rsc.li/materials-a

View Article Online
DOI: 10.1039/D6TA00999A

From Plastic Waste to Value-Added Chemicals: A Trimetallic MOF Strategy for Electrochemical PET Upcycling

Divy G. Solanki[1], Pooja J. Sharma[1], Sanjay A. Bhakhar[1], Manish N. Nandpal[2], Samir G. Patel[2], Chakkooth Vijayakumar[3], Sudhanshu Sharma[4], C.K. Sumesh[1], Pratik M. Pataniya[1*]

[1]*Department of Physical Sciences, P. D. Patel Institute of Applied Sciences, Charotar University of Science & Technology, CHARUSAT, Changa, India-388421.*

[2]*Department of Pharmaceutical Chemistry and Analysis, Ramanbhai Patel College of Pharmacy, Charotar University of Science and Technology, CHARUSAT Changa-388421, India.*

[3]*Chemical Sciences and Technology Division, CSIR-National Institute for Interdisciplinary Science and Technology (NIIST), Thiruvananthapuram-695 019, India.*

[4]*Department of Chemistry, Indian Institute of Technology Gandhinagar, Palaj, 382355, India.*

[*]**Email:** pm.pataniya9991@gmail.com

View Article Online
DOI: 10.1039/D6TA00999A

Abstract:

Electrocatalytic upcycling of polyethylene terephthalate (PET) plastics into value-added chemicals provides a sustainable route to simultaneously mitigate plastic pollution and enable energy-efficient chemical synthesis. Herein, we develop a tri-metallic NiMnCo metal–organic framework (NiMnCo-MOF) as a highly efficient electrocatalyst for advanced oxidation of PET-derived ethylene glycol (EG). As compared to pristine Co-MOF, the incorporation of Ni and Mn induces a pronounced morphological evolution, yielding ultrathin, loosely interwoven nanosheet architectures with abundant exposed edges and hierarchical porosity. Additionally, the modulated electronic structure of the metal centers facilitates the significant reduction in charge-transfer resistance and increases the electrochemically active surface area, thereby accelerating reaction kinetics. Consequently, the NiMnCo-MOF offers a Faradaic efficiency of 98% for selective EG-to-formate conversion, demonstrating excellent activity and selectivity under alkaline conditions. Importantly, terephthalate (TPA) recovered from PET hydrolysate is successfully reused as a linker to synthesize Co-MOF, which exhibits electrochemical performance comparable to that of Co-MOF derived from commercial TPA, highlighting the intrinsic recyclability of the catalyst-plastic system. These findings advocate a closed-loop strategy integrating plastic waste valorization, multimetal MOF engineering, and efficient electrochemical conversion, offering fundamental insights for the rational design of advanced catalysts toward sustainable energy and environmental applications.

Keywords: Electrocatalytic PET upcycling; multi-metal MOF; ethylene glycol oxidation; circular chemistry; electronic structure modulation.

View Article Online
DOI: 10.1039/D6TA00999A

Introduction:

Polyethylene terephthalate (PET) is among the most extensively produced and consumed plastic, with widespread applications in beverage bottles, packaging films, textiles and engineering materials. Its large-scale industrial adoption is driven by advantages such as high chemical stability, mechanical strength, optical transparency, and low-cost. However, strong ester bonds and aromatic structure of PET make it difficult to degrade naturally, leading to persistent environmental accumulation. Fortunately, PET can be hydrolysed into its monomers, ethylene glycol (EG) and terephthalate (TPA) owing to its polyester nature[1–5]. In this context, electrocatalytic upcycling of PET has emerged as a promising technique, which offers dynamic regulation of reaction pathways, eliminates harsh reagents, and allows coupling with renewable energy sources. Importantly, electrocatalytic oxidation of PET-derived EG can be coupled with hydrogen evolution reaction or CO_2 reduction reaction at the cathode, creating dual-functional systems that simultaneously address plastic waste valorization and sustainable energy generation[6,7].

Electro-oxidation of PET-derived EG has gained significant attention as EG serves as a highly reactive feedstock for synthesis of value-added chemicals such as glycolic acid, glyoxylic acid, oxalic acid, and formate, depending on the reaction conditions and catalyst surface properties[8–10]. However, the multi-electron transfer pathways involved in C–C and C–H bond cleavage often lead to complex reaction pathways, making it difficult to control product distribution. The strong adsorption of EG on metal surfaces causes the poisoning effects that degrade catalyst performance over prolonged operation. Additionally, the sluggish kinetics of alcohol oxidation in alkaline media and competition between EG oxidation reaction (EGOR) and oxygen evolution reaction (OER) further hinders the efficiency. It demands the electrocatalysts with abundance of active sites for highly selective EGOR[11].

View Article Online
DOI: 10.1039/D6TA00999A

Generally, the electrocatalysts based on transition metals such as nickel (Ni)[12–13], cobalt (Co)[14–16], iron (Fe)[8], and manganese (Mn)[17] have been widely identified as electrocatalysts for highly selective advanced oxidation reactions due to their earth abundance, tunable electronic structure, tunable surface-morphology and favorable adsorption energetics for organic intermediates. Particularly, Ni and Co-based catalysts facilitates the superior advanced oxidation reaction owing to dynamic formation of metal oxy-hydroxides (MOOH) sites in alkaline condition[18–20]. The in-situ formed MOOH centres facilitates the chemical-oxidation (in-direct alcohol oxidation mechanism) of EG[21,22]. Moreover, Mn-based catalysts display strong oxygen-binding and lattice-oxygen participation, which can open additional oxidation pathways, although stability may become a concern[17]. The growing interest in bi-metallic and tri-metallic catalysts stems from the importance of electronic-structure modulation, where the interaction between different metal centers can alter d-band occupancy, charge distribution, and surface adsorption strengths[23,24]. Such optimized catalytic nanostructures can suppress unwanted side reactions, and improve tolerance against poisoning intermediates.

Metal–organic framework (MOF)-derived catalysts have attracted considerable attention in electrochemical oxidation due to their intrinsic porosity, tunable composition, and ability to form well-dispersed metal/metal-oxide nanostructures upon thermal or chemical transformation[25–27]. Additionally, MOFs offers ordered pore networks, and controllable metal–ligand environments that can be engineered to introduce active centers with tailored electronic structures[28,29]. The MOFs also undergo surface-reconstruction during electrolysis in alkaline condition due to weaker coordination between metal nodes and organic linkers, leading to the formation of metal hydroxides and oxy-hydroxides on the surface[30,31]. Although, these reconstructed layers are typically real active sites for advanced oxidation, the excess degradation leads to metal leaching and collapse of the porous architecture[32]. E.g.

View Article Online
DOI: 10.1039/D6TA00999A

Co-MOF suffers from corrosion during oxidation reaction in alkaline condition and demonstrates the morphological evolution from its original microfiber morphology to nanosheets[33]. Zhong *et al* demonstrated the stability of Co-MOF during electro-oxidation by incorporation of Ni^{2+} by regulating the dissolution-redeposition mechanism[33]. Therefore, the MOFs with multi-metallic sites are highly required for controlled surface reconstruction and modulated electronic structure, leading to energy efficient as well as sustainable up-cycling of PET technology.

Motivated by this, we developed the NiMnCo-MOF nanostructured catalysts with modulated electronic structure and surface morphology. Compared to pristine Co-MOF, NiMnCo-MOF with optimization of molar ratio of Ni and Mn (Ni:Mn = 1:1, 1:2 and 2:1) demonstrated thin nanosheets with rough terrace and vertical orientation, enabling the exposure of more active sites. The controlled surface re-construction, as studied by in-situ Raman spectroscopy confirms the formation of NiOOH and CoOOH sites on surface of NiMnCo-MOF, facilitating the chemical-oxidation of the EG via indirect-alcohol oxidation mechanism. Owing to superior catalytic performance of NiMnCo-MOF towards EGOR, we demonstrated the up-cycling of real PET bottle waste into TPA and formate (FA). The highly selective EG to FA conversion with Faradaic efficiency of 98% have been achieved due to effective suppression of conventional OER. The recovered TPA was further utilized for synthesis of Co-MOF, which exhibits the identical vibrational and structural properties and Electrocatalytic PET upcycling performance as compared to Co-MOF prepared from commercial TPA. Present research advocates a novel idea to design efficient MOF structures for efficient and sustainable electrocatalysis.

View Article Online
DOI: 10.1039/D6TA00999A

Experimental:

Synthesis of Co MOF@NF:

NF (3×3 $cm^{2)}$ was cleaned by water and acetone, followed by sonication in 2.5M HCl for about 15 minutes. After sonication NF was washed with water to remove HCl. A precursor solution containing 1.16 g Co $(NO_3)_2 \cdot 6H_2O$ and 0.132g of PVP in 20 mL Distilled water (solution-1) was prepared. Meanwhile, 0.21g of TPA was dissolved into 20 mL of DMF (solution-2). Then, both solutions were mixed and stirred for 20 minutes. The final precursor solution along with pre-treated NF were transferred into SS-lined Teflon autoclave (capacity: 100 ml) and heated at 160°C for 15 hours. Then, the Co-MOF electrode was collected and washed using water and acetone. The cleaned Co-MOF electrode was finally dried at 70°C for 5 hours in vacuum oven (~10^{-3} torr).

Synthesis of NiMnCo-MOF and NiMn electrodes:

A precursor solution containing different concentrations of $NiSO_4.6H_2O$ and $MnSO_4$ $.H_2O$ were prepared in 40 mL of distilled water. Then, the $CO(NH_2)_2$ (0.0280 g) and NH_4F (0.0058g) was added in the precursor solution. The final solution was stirred for 20 minutes. The precursor solution along with Co-MOF@NF electrode were transferred into SS-lined Teflon autoclave (capacity: 100 ml) and heated at 120°C for 12 hours. Then, the prepared NiMn@Co-MOF electrode was cleaned using water and acetone. The prepared electrode was dried at 70°C for 5 hours in vacuum oven (~10^{-3} torr). The electrodes with different Ni/Mn molar ratio such as (1:1), (1:2) and (2:1) were synthesized and labelled as NiMnCo-1, NiMnCo-2 and NiMnCo-3. The NiMn@NF electrode was synthesized with identical precursor solution and method on bare NF.

View Article Online
DOI: 10.1039/D6TA00999A

Result and Discussion:

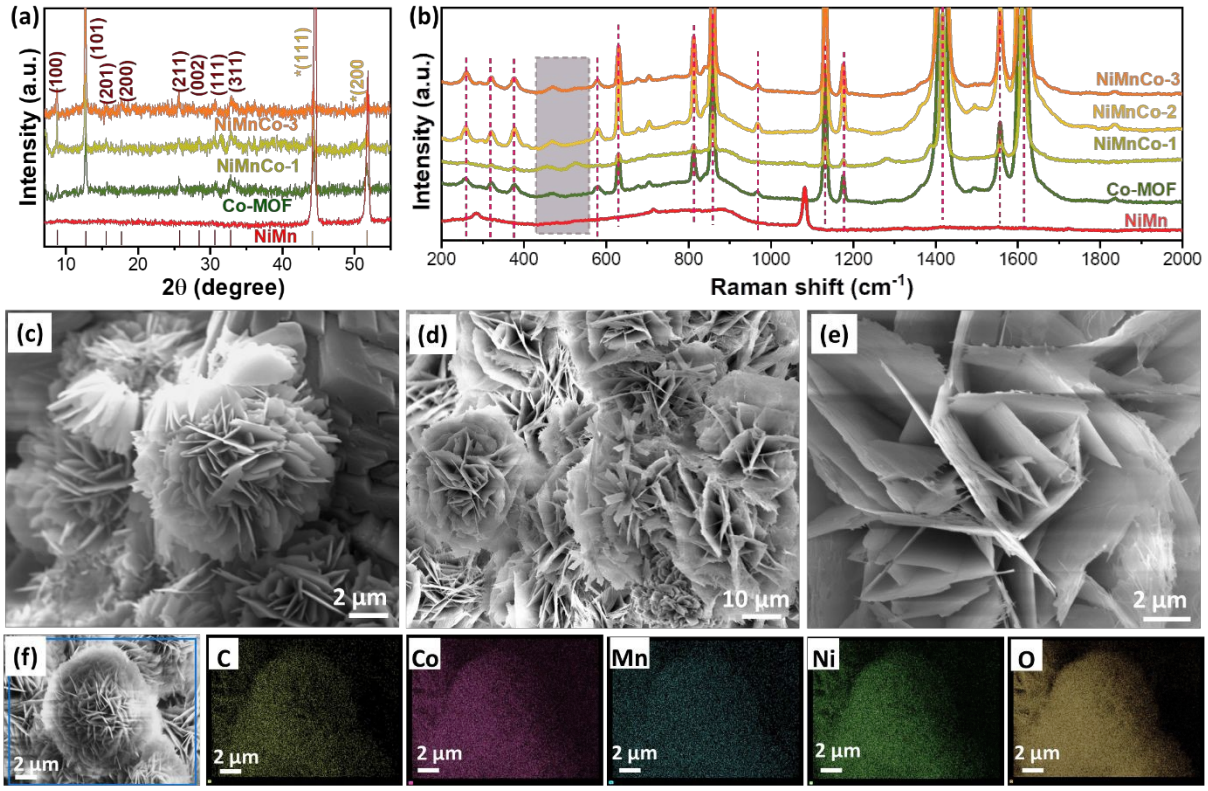

Figure 1 (a) Powder XRD patterns of NiMn_LDH, NiMnCo, NiMn-LDH and Co-MOF catalysts, (b) Raman spectra of NiMn, NiMnCo-MOF and Co-MOF electrodes, (c) SEM image of Co-MOF (d,e) SEM images of NiMnCo-1 catalyst, (f) EDS-elemental mapping of NiCoMn-1 catalyst.

The NiMn@Co-MOF (e.g. NiMnCo-1, NiMnCo-2, NiMnCo-3), Co-MOF and NiMn LDH electrodes were synthesized using two-step hydrothermal technique and used for PET electro-upcycling. Firstly, the structure of NiMnCo-1, NiMnCo-2, NiMnCo-3 and Co-MOF was investigated using powder XRD (**Figure 1-a**). The XRD pattern of Co-MOF shows diffraction peaks at 8.79°, 12.85°, 15.67°, 17.92°, 25.63°, 28.55°, 30.69° and 32.80°, which are well-indexed to (100), (101), (201), (200), (211), (002), (111) and (311), crystallographic planes of Co-MOF, respectively[21,34]. The XRD patterns of NiMnCo-1, NiMnCo-2 and NiMnCo-3 also exhibited the similar peaks, attributing the retention of Co-MOF structure after second step of synthesis. Additionally, the peaks corresponding to 45.5° and 52.98° corresponding to (111) and (200) planes of Ni foam(JCPDS- 04-0850) [35]. Furthermore, the

View Article Online
DOI: 10.1039/D6TA00999A

Raman spectroscopy provides the crucial vibrational insight into the structural transformations and chemical speciation occurring within the Co-MOF. As shown in **Figure 1-b**, the Raman spectra of Co-MOF shows the characteristic peaks organic benzene-1,4-dicarboxylate (BDC) linkers. The peaks 636 cm^{-1}, 815 cm^{-1} and 866 cm^{-1} attributed to aromatic C-H bond [36]. While, the peaks at 1423 cm^{-1}, 1564 cm^{-1}, and 1616 cm^{-1} for Co-BDC are assigned to symmetric (ν_s) and asymmetric (ν_{as}) (-COO−) vibrations[37]. The peaks due to O–C–O bending of –COOH (258 cm^{-1}) aromatic ring torsion (321 cm^{-1} and 377 cm^{-1}) are also observed. Additionally, a weak peaks at 470 cm^{-1} (E_g) and 523 cm^{-1} (F_{2g}) are assigned to Co-O-Co bending and confirms the metal hydroxide phase[38].

Further, SEM images demonstrate the morphological evolution in Co-MOF and NiMnCo-1 MOF. **Figure 1-c** shows the SEM image of Co-MOF, showing the formation of well-defined, flower-like microstructures assembled from radially oriented ultrathin nanosheets. These partially spaced separated nanosheets in the micro-flower provides the open channels throughout architecture, facilitating higher surface area. After NiMn-incorporation, the flower-like morphology is retained, suggesting the structurally robustness of Co-MOF during secondary hydrothermal treatment (**Figure 1-d**). However, the noticeable increase in the surface roughness is realised for NiMnCo-1 MOF. The NiMnCo-1 MOF exhibited thinner and sharper-edged stacked nanosheets as compared to Co-MOF (**Figure 1-e**), facilitating higher open interlayer spacing, which may enhance the ionic-diffusion to facilitate enhanced electrochemical performance. SEM-EDS elemental mapping demonstrates the presence of elements (Co, Mn, Ni, O and C) of NiMnCo-1 MOF (**Figure 1-f**) **(Figure S1, supporting information)**. The structure and morphology of the NiMnCo-1 was further investigated using HR-TEM. The TEM image shows the nanosheets like morphology of NiMnCo-1 electrocatalysts (**Figure S2-a**). **Figure S2-b** shows the region with d-spacing 0.29 nm, which is assigned to (111) plane. The surface area and pore size distribution of NiMnCo-1 catalyst

View Article Online
DOI: 10.1039/D0TA00999A

was further analysed using Brunauer-Emmett-Teller (BET) analysis. The nitrogen gas adsorption-desorption isotherm exhibits hysteresis loop attributes to the mesoporous nature of NiCoMn-1. (**Figure S3**) [39,40]. The specific area is found to be 8.75 m^2/g from BET analysis, while, the pore diameter measured by the Barret-Joyner-Halenda (BJH) technique is 205 Å.

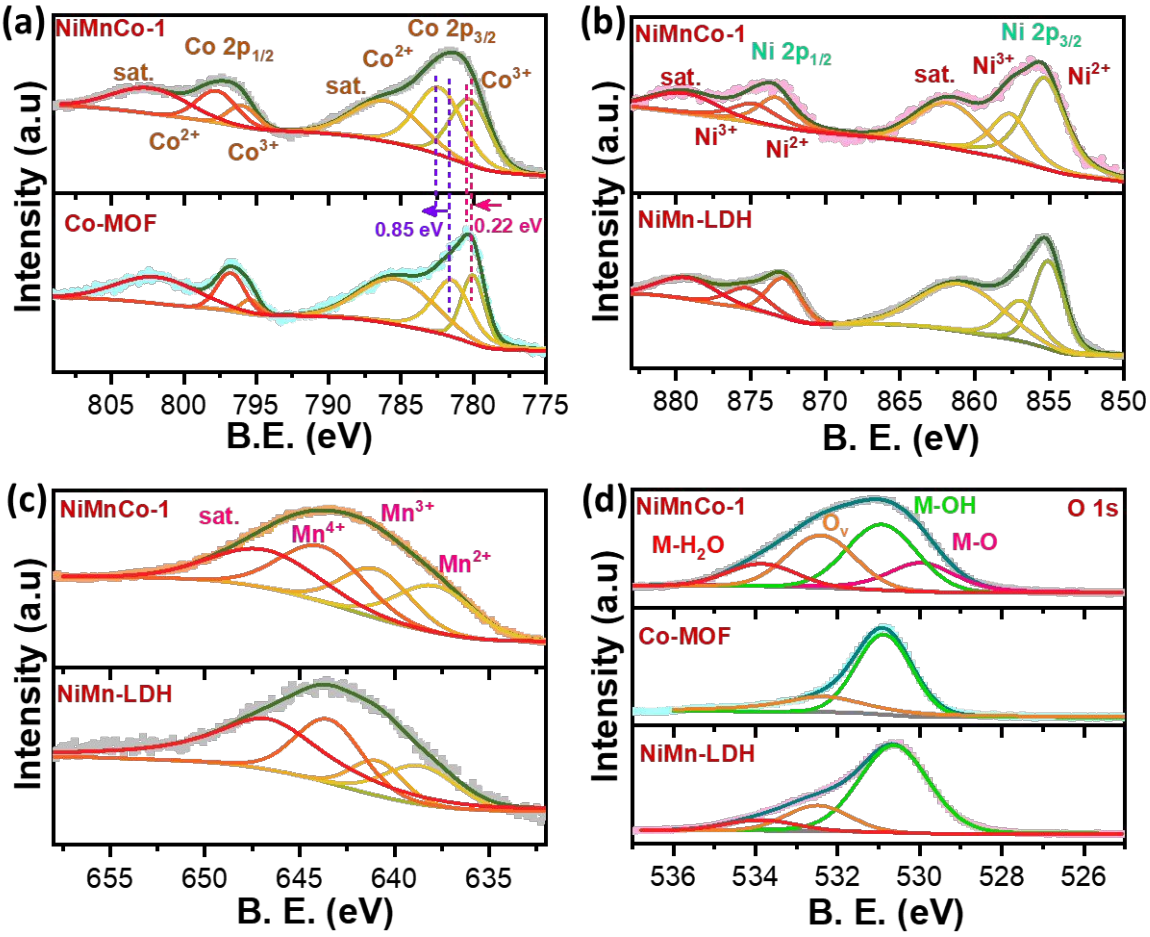

Figure 2 XPS survey of NiMn-LDH and NiMnCo-1 catalyst, (a) Ni 2p, (b) Mn 2p, (c) O 1s and (d) Co 2p.

The X-Ray photoelectron spectroscopy (XPS) was carried out to investigate the chemical state and valance states of elements of the Co-MOF, NiMnCo-1 and NiMn-LDH based electrocatalysts. As shown in **Figure 2-a**, Co 2p XPS spectra shows the spin-orbital doublet of Co^{3+} and Co^{2+} electronic states. The deconvoluted peaks located at 780.66 eV and 795.97 eV corresponds to Co^{3+} electronic state, while, the peaks located at 781.86 eV and

View Article Online
DOI: 10.1039/D6TA00999A

797.73 eV are assigned to Co^{2+}-state in NiMiCo-1. Additional peaks centred at 786.03 eV and 802.33 eV are shake-up satellite peaks. Importantly, Co 2p XPS peaks of NiMnCo-1 exhibits the positive binding energy shift, showing the strong coupling of Ni and Mn elements with Co and decrease in electronic density around Co-sites[41]. Additionally, Co^{3+}/Co^{2+} ratio is enhanced from 0.63 for Co-MOF to 0.77 for NiMnCo-1, demonstrating the oxidation of Co^{2+} to Co^{3+} due to incorporation of NiMn in electrocatalysts[42]. The Ni 2p XPS survey exhibits the peak deconvoluted peaks at 855.32 eV and 873.30 eV, assigned to Ni $2p_{3/2}$ and Ni $2p_{1/2}$ of Ni^{2+}-state (**Figure 2-b**). The peaks at binding energy 857.61 eV and 874.80 eV corresponds to Ni^{3+}-electronic state[43]. The Ni^{3+}/Ni^{2+} ratio is reduced from 0.63 for NiMn-LDH to 0.47 eV for NiMnCo-1, showing the reduction of Ni^{3+} to Ni^{2+} due to strong coupling with Co-sites. **Figure 2-c** shows the Mn 2p XPS survey, exhibiting at peaks at binding energies 637.85 eV, 640.96 eV and 643.81 eV are assigned to Mn $2p_{3/2}$ of Mn^{2+}, Mn^{3+} and Mn^{4+} electronic states in NiMnCo-1[44]. Apart from synergistic coupling of metal sites and co-existence of multivalent metallic sites, O 1s XPS survey of demonstrates the increase in the concentration of oxygen vacancies (532.40 eV) in NiMnCo-1 (**Figure 2-d**)[45,46]. Additionally, the peaks centred at 529.96 eV, 530.93 eV and 533.85 eV corresponds to M-O, M-OH and M-H_2O interactions, respectively[8].

Oxygen Evolution Reaction, EGOR and POR:

The electrochemical performance of oxygen evolution reaction (OER) and ethylene glycol oxidation reaction (EGOR) of NiMnCo-1, NiMnCo-2, NiMnCo-3, Co-MOF, NiMn-LDH electrodes was studied in alkaline electrolyte (1M KOH). **Figure 3-a** shows the iR-compensated polarization curves of OER and EGOR of NiMnCo-1, NiMnCo-2, NiMnCo-3, Co-MOF, NiMn-LDH electrodes. The typical oxidation peak was observed in polarization curves of OER for all the catalysts, which is observed due to oxidation of metallic sites (Co^{+2} to Co^{+3} and Ni^{+2} to Ni^{+3}). As observed the incorporation of Co has significantly shift the

View Article Online
DOI: 10.1039/D0TA00999A

oxidation peak of Ni towards lower potential region[41]. With optimized chemical composition, NiMnCo-1 electrode shows the superior electrochemical OER performance and requires anodic potential of 1.47 V vs RHE to reach the current density of 100mA/cm^2 which is lower than NiMnCo-2 (1.51 V vs RHE), NiMnCo-3 (1.51 V vs RHE), NiMn-LDH (1.68 V vs RHE) and Co-MOF (1.54 V vs RHE) (**Figure 3-b**). The catalytic OER performance of NiMnCo-1 is superior as compared to bi-metallic MOF such as NiCo-MOF and MnCo-MOF (**Figure S4-a**). The oxygen evolution reaction in alkaline media is complex four electron process (**equ.: 1-4**):

$$*M + OH^-(aq) \rightarrow *MOH_{ads} + e^- \quad \text{----------(1)}$$

$$*MOH_{ads} + OH^-(aq) \rightarrow *MO_{ads} + H_2O + e^- \quad \text{----------(2)}$$

$$*MO_{ads} + OH^-(aq) \rightarrow *MOOH_{ads} + H_2O + e^- \quad \text{----------(3)}$$

$$*MOOH_{ads} + OH^-(aq) \rightarrow *M + O_2 + H_2O + e^- \quad \text{----------(4)}$$

To study the kinetics of the OER activity and rate determining step, the Tafel slope is also calculated for all the electrodes (**Figure 3-c**). Encouragingly, NiMnCo-1 electrodes exhibited lowest value of Tafel slope (113 mV/dec), showing its faster reaction kinetics and improved kinetics to adsorb OH^- from electrolyte on the surface of M* as compared to other electrodes[47].

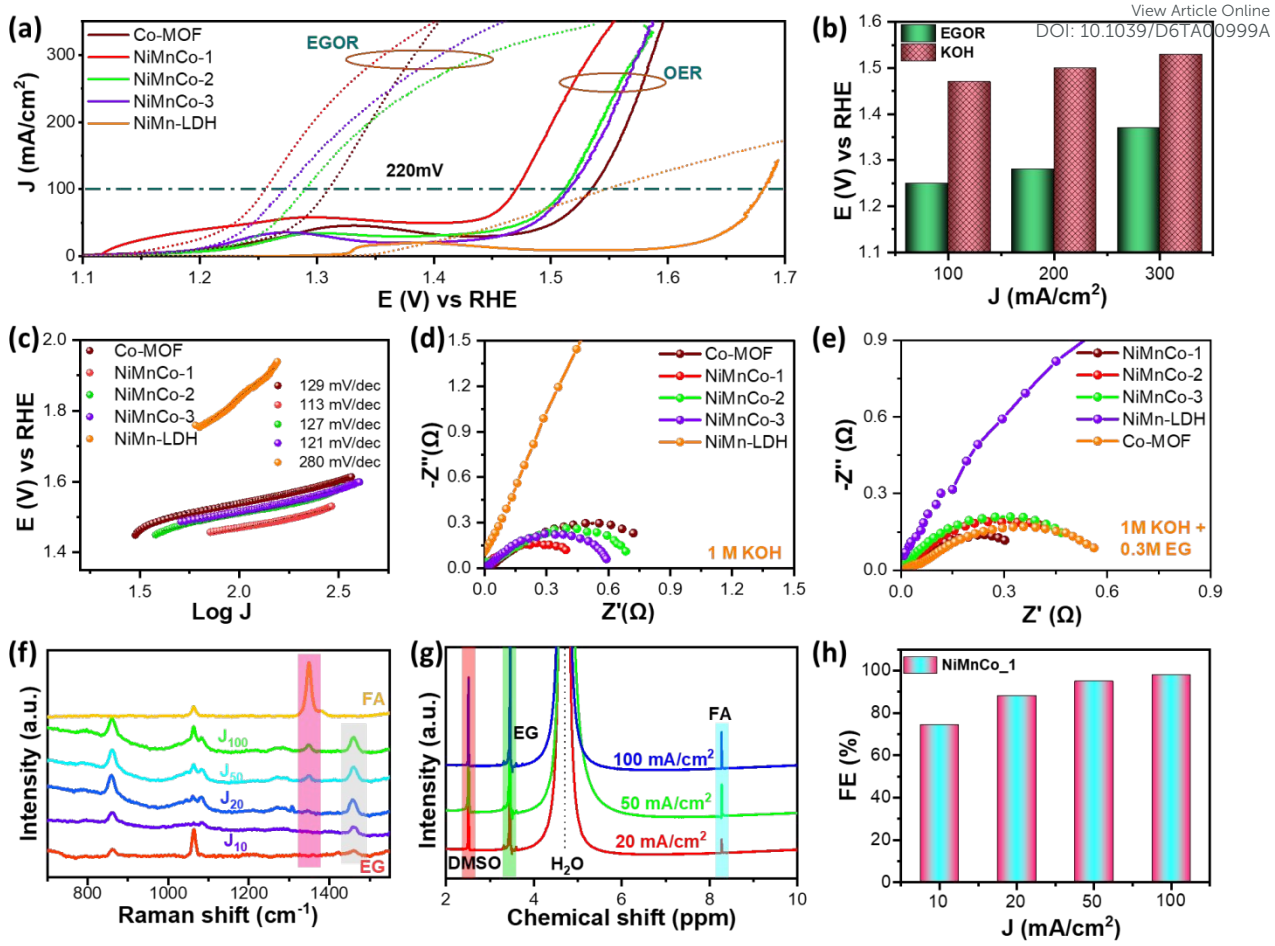

Figure 3 (a) Polarization curves for Co-MOF, NiMnCo and NiMn-LDH based catalysts in 1 M KOH (OER) and 1 M KOH + 0.3 M EG (EGOR) with iR compensation, (b) Anodic potential to deliver 100 mA/cm^2, 200 mA/cm^2 and 300 mA/cm^2 for OER and EGOR on NiMnCo-1 catalyst, (c) Tafel plots for OER, (d) Nyquist plot at 1.5 V vs RHE in 1 M KOH, (e) Nyquist plot at 1.4 V vs RHE in 1 M KOH + 0.3 M EG, Analysis of EG electrolyte after electro-oxidation for 2 hr at different current densities, (f) Raman spectra, (g) ^{1}H NMR spectra, and (h) Calculation of Faradaic efficiency for production of formate at different current densities (Electrolysis time = 2 hr).

Although, the anodic OER activity is environmentally beneficial, its higher overpotential lower the efficiency and increases the cost of catalysis cell. PET (Polyethylene Terephthalate) after alkaline hydrolysis can be depolymerized into its monomers EG and TPA. One of the energy-efficient advanced oxidation reactions, the EGOR have much lower thermodynamic potential (0.57 V vs RHE) as compared to OER (1.23 V vs RHE). To reduce energy consumption and to promote plastic waste upcycling, we examined EGOR (1 M KOH + 0.3 M EG) and PET plastic hydrolysate oxidation reaction (POR) on NiMnCo-1, NiMnCo-2, NiMnCo-3, Co-MOF, NiMn-LDH electrodes. Polarization curves for EGOR demonstrates that NiMnCo-1 electrode shows the superior catalytic performance, generating current density

View Article Online
DOI: 10.1039/D0TA00999A

of 100 mA/cm^2 at potential of 1.25 V vs RHE which is lower as compared to anodic potential for NiMnCo-2 (1.29 V vs RHE), NiMnCo-3 (1.27 V vs RHE), NiMn-LDH (1.54 V vs RHE) and Co-MOF (1.32 V vs RHE). The synergistic combination of metallic sites in NiMoCo-1 leads to superior EGOR catalytic performance compared to mono-metallic (Co-MOF) and bi-metallic MOF (NiCo-MOF and MnCo-MOF) (**Figure S4-b**). Encouragingly, the energy-efficient behaviour of EGOR reduces the anodic potential by 220 mV at 100 mA/cm^2 current density as compared to conventional OER. The interfacial charge transfer was further analysed for all the electrodes using EIS. Encouragingly, NiMnCo-1 electrodes exhibited lowest charge-transfer resistance for OER as well as EGOR (**Figure 3-d,e,S5**), showing its accelerated interfacial charge-transfer due to regulated charge-transport and synergistic charge transfer mechanism[48]. The double layer capacitance (C_{dl}), specific capacitance (C_s) and electrochemically active surface area (ECSA) were further evaluated[49]. The cyclic-voltametry curves recorded in non-faradaic region at different scan rate (10-100 mV/s) (**Figure S6-a,b**). The C_{dl} is evaluated to be 0.11 mF/cm^2 for Co-MOF and 0.49 mF/cm^2 for NiMnCo-1 (**Figure S6-c**). While, the Cs is found to enhanced form 0.09 mF/cm^2 for Co-MOF to 0.39 mF/cm^2 for NiMnCo-1(**Figure S6-d**). The ECSA for NiMnCo is slightly enhanced for NiMnCo-1 (1.26 cm^2) compared to Co-MOF (1.22 cm^2). Apart from these, **Figure S7** shows ECSA normalized polarization curves to analyse intrinsic improvement in catalytic performance.

The product analysis of the oxidation of EG after electrolysis for 2 hours at different current density was further conducted by Raman spectroscopy (**Figure 3-f**). The Raman spectra of the control EG electrolyte shows the characteristic peaks due to stretching vibrations of C–C bond (861 cm^{-1}), C–O bond (1064 cm^{-1}) and C–H bond (1460 cm^{-1}) [50,51]. The emergence of new peak at 1349 cm^{-1} after electrolysis shows the conversion of the EG to FA (due to C-H bending vibration of FA) [52,53]. The intensified peak of FA suggests the increase in the

View Article Online
DOI: 10.1039/D6TA00999A

amount of FA, along with the original peaks of EG. The ^{1}H NMR spectroscopy was further conducted for the analysis of oxidation product (**Figure 3-g**). The ^{1}H NMR spectra shows the presence of remaining EG at 3.44 ppm and formate (FA) at 8.28 ppm. While, the peak at 2.51 ppm can be observed due to DMSO (internal standard). The signal of the FA increases significantly on increasing the electrolysis current density from 10-100 mA/cm^2. The amount of the formate was measured using standard curve method using HPLC technique **(Table S1, Figure S8-10**). The formate production rate increases from 0.092 m mol/hr at 10 mA/cm^2 to 1.218 m mol/hr at 100 mA/cm^2 (**Table S2**). The Faradaic efficiency of NiMnCo-1 for conversion from EG to FA is 98% at optimum current density of 100 mA/cm^2 (**Figure 3-h**). **Figure S-11** demonstrates the alkaline EGOR pathway proceeding via an indirect alcohol-oxidation mechanism. Firstly, ethylene glycol is oxidized to glycolaldehyde through a two-electron dehydrogenation step. The formed glycolaldehyde subsequently follows two parallel routes: (i) oxidation to glycolic acid and further to formate with partial C–C bond cleavage (major-step), (ii) oxidation to glyoxal followed by oxidative C–C cleavage yielding formate (minor). Both the step involves hydroxide-assisted two-electron transfers, which are kinetically more favourable than conventional OER. The controlled stepwise oxidation of EG efficiently suppresses over-oxidation and enables high selectivity toward formate formation[8,22].

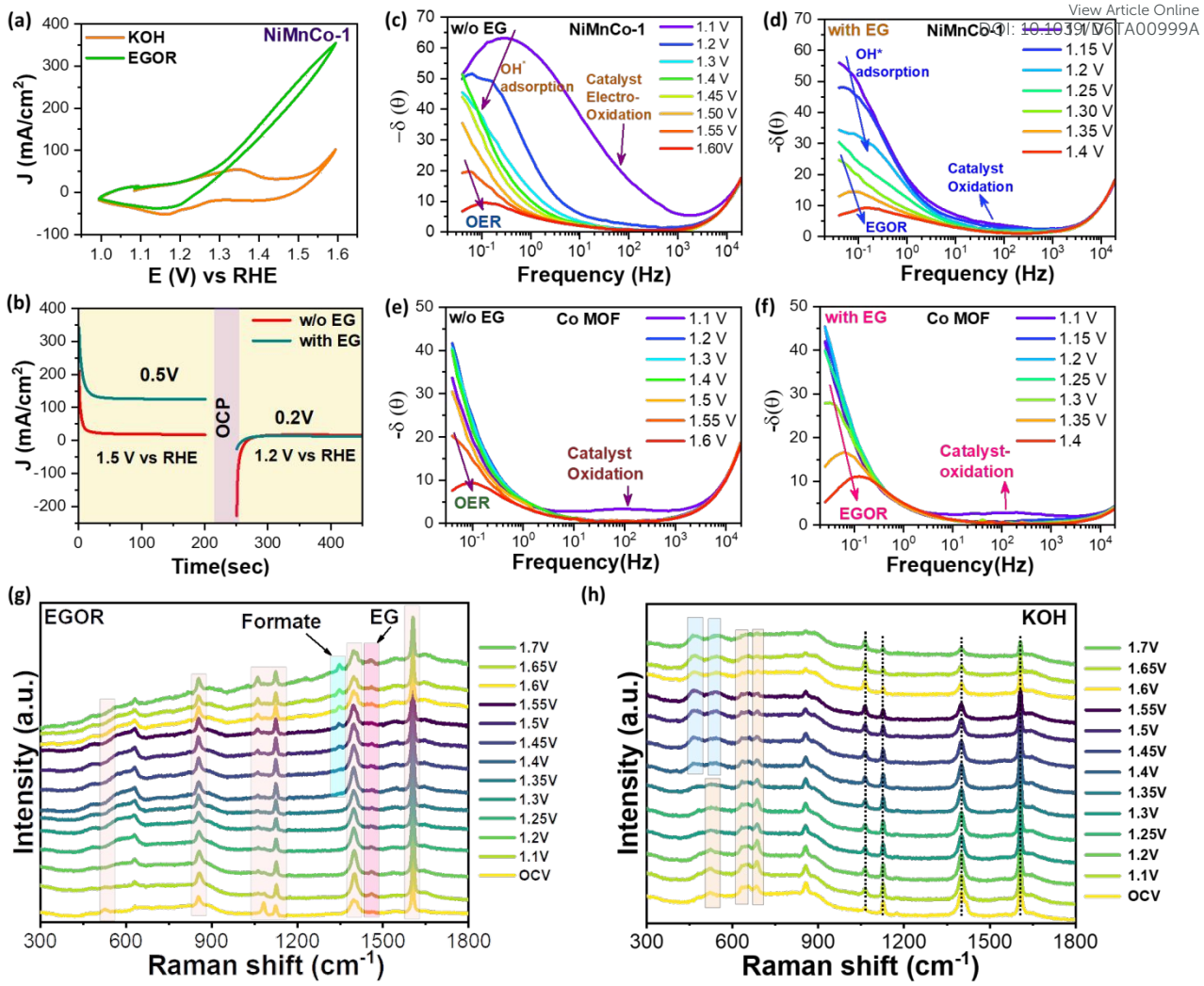

Figure 4 (a) CV curves of NiMnCo-1 in EGOR and OER, (b) chrono-amperometry test in 1M KOH electrolyte with and w/o EG, (c,d) Bode plot of NiMnCo-1 in KOH with and without (w/o) EG, (e, f) Bode plot of Co-MOF in KOH with and without (w/o) EG, (g, h) In-situ Raman spectra at different potential of NiMnCo-1 in KOH with and without (w/o) EG.

To gain deeper insight into the EGOR, chrono-amperometry tests were conducted at 1.5 V vs RHE and 1.2 V vs RHE in 1.0 M KOH, both with and without 0.3 M EG. Without EG (**Figure 4-b**), a distinct anodic current at 1.5 V vs RHE is attributed to the surface re-construction due to electrochemical oxidation of transition metal sites, forming catalytically active metal oxyhydroxide (MOOH) species through reaction [M–OH → MOOH + e^-] [13,24]. While with EG addition, the anodic current increases significantly, indicating that EG undergoes rapid electrochemical oxidation, facilitated by its chemical interaction with MOOH centres. This reaction likely involves nucleophilic attack by EG on MOOH, leading to C–C

View Article Online
DOI: 10.1039/D5TA00999A

bond cleavage and formation of oxidation intermediates[54]. When 1.2 V is applied in step-CA test, the obvious reduction current can be seen, indicating the reduction of MOOH sites into M-OH sites. While, the reduction current is suppressed with EG in electrolyte, suggesting that MOOH is chemically consumed during EG oxidation[54]. This behaviour supports a coupled electrochemical-chemical (EC) mechanism, where MOOH acts as both an electro-generated oxidizing agent and a reactive intermediate [54]. The dynamic balance between MOOH formation and consumption governs the overall EGOR efficiency. Such mechanistic understanding is crucial for designing advanced electrocatalysts with tailored redox properties. Moreover, the suppression of cathodic current shows the chemical reduction pathway of MOOH by EG. Cyclic-voltammetry tests in potential range 1 to 1.6 V vs RHE shows that the onset-of EGOR is nicely overlapping with the onset of the typical oxidation peak (**Figure 4-a, S12-a**), which is associated with the oxidation of metallic sites and the significant reduction in the reduction current in electrolyte with EG supports the EC-mechanism for EGOR [54].

The dynamics of OER and EGOR activity and surface-reconstruction on catalyst was further studied by in-situ operando EIS spectroscopy. **Figure 4-c-f** shows potential dependent Bode plot of NiMnCo-1 and Co-MOF in alkaline electrolyte with and without EG in frequency range of 10^5 Hz to 0.01Hz. For NiMnCo-1 and Co-MOF, a progressive decrease in phase angle is observed at low frequencies as the applied potential increases. This decreasing trend suggests that charge-transfer kinetics become faster at higher potentials, leading to lower interfacial resistance and more efficient electron transfer between the catalyst and electrolyte. Such behaviour is typical for active OER catalysts, where enhanced surface oxidation and activation of metal sites improve reaction kinetics at elevated potentials. In the case of ethylene glycol oxidation (EGOR), the phase response behaves differently. The Bode plots reveal an electro-oxidation signature appearing earlier at mid-frequency regions, occurring before the low-frequency OER features dominate. This indicates that surface oxidation during EGOR initiates

View Article Online
DOI: 10.1039/D6TA00999A

prior to OER and involves distinct reaction intermediates that influence the electrochemical impedance. As the potential further increases, the EGOR peaks shift toward lower frequencies while maintaining reduced phase angles, implying faster electron transfer and improved oxidation kinetics. Overall, NiMnCo-1 consistently displays lower phase angles than Co-MOF across all examined potentials and catalytic conditions, demonstrating superior catalytic activity and interfacial charge-transfer characteristics in both EGOR and OER.

Real-time insights into surface chemistry were obtained using in-situ operando Raman spectroscopy in 1M KOH with and without 0.3M EG (**Figure 4-g,h**,**S12-b**) in potential range 0.1–0.7V to study the ligand dynamics and metallic phase evolution. Firstly, the Raman spectra of NiMnCo-1 electrode at open circuit potential (OCP) in 1M KOH with and without EG shows the presence of terephthalate linkers with coordination to metal centres. As the potential is increased from 1.1 V vs RHE, the OH^- present in electrolyte starts to break the metal carboxalate ligands (M-O-C) linkages, leads to disappearance of 689 cm^{-1} wagging, C–C and COO^- stretching, marks the onset of MOF reconstruction[55]. At higher potentials, breaking of ligand coordination bond opens the Co and Ni sites for oxidation to produces hydroxide and oxy-hydroxide[55]. At potential 1.3 V vs RHE, the emergence of Raman peaks at 463 cm^{-1} and 639 cm^{-1} indicates the formation of CoOOH[55]. While on exceeding potential above 1.4 V vs RHE, the formation of Raman peaks centered at 489 cm^{-1} (E_g mode) and 544 cm^{-1} (F_{1g} mode) confirms the formation of NiOOH sites (**Figure 4-h**)[33,55]. In-situ Raman spectroscopy was performed to study the pathway of conversion of EG to formate and surface reconstruction. In addition to characteristic peaks of NiMnCo-1, Raman spectra show the additional peak at 1460 cm^{-1} owing to presence of the EG in electrolyte (**Figure 4-g**). When the potential is increased above 1.30 V vs RHE, the emergence of a peak at 1350 cm^{-1} confirms the conversion of EG to formate. Additionally, the intensity this peak increased on increasing the potential, indicating the enhanced rate of EGOR[52]. Absence of peaks of metal oxy-hydroxide (MOOH) in Raman

View Article Online
DOI: 10.1039/D6TA00999A

spectroscopy for NiMnCo-1 in EG electrolyte further suggests the consumption of MOOH sites by chemical oxidation of EG, confirming the indirect-alcohol oxidation mechanism of EGOR on NiMnCo-1 electrode[8,22].

PET electro-upcycling:

By knowing the superior EGOR performance, NiMnCo-1, NiMnCo-2, and NiMnCo-3 electrodes were further explored for electro-upcycling of the real PET plastic waste. The NiMnCo-1 shows the superior POR activity compared to control electrodes, generating current density of more than 300 mA/cm^2 (**Figure 5-a, S4-c**). Encouragingly, the catalytic performance of NiMnCo-1 is superior as compared to transition metal based state-of-the-art catalysts (Table S3). At current density of 100 mA/cm^2, NiMnCo-1 requires an anodic potential of 1.25 V vs RHE, achieving a potential difference of 220 mV as compared to OER, indicating the highly selective oxidation of PET derived EG and enabling the electro-upcycling of plastic at industrially large current densities (> 300 mA/cm^2). The ^{1}H NMR spectra further shows the presence of EG and TPA after alkali-hydrolysis of PET waste and also shows the conversion of PET derived EG into FA (**Figure 5-b**). To extend the economic potential of the electrocatalytic upcycling of PET waste, we have demonstrated the separation of TPA and formate after electrolysis of PET hydrolysate (**Figure 5-d**). After complete electrolysis, the electrolyte was acidified (pH ~ 3) by adding excess formic acid for the precipitation of TPA. After separation of TPA by centrifugation, formate was recycled though crystallization from the remaining electrolyte. The recycled TPA was investigated by Raman spectroscopy (**Figure 5-c**), showing the characteristic peaks which are well matched with that of commercial TPA. As shown in **Figure 5-d$_1$**, the recovered TPA was utilized further for the synthesis of Co-MOF. The Co-MOF synthesized from recovered TPA (labelled as R-Co MOF) exhibits the vibrational modes identical to original Co-MOF (synthesized using standard TPA). Encouragingly, the R-Co MOF and Co MOF exhibited the comparable OER and EGOR

View Article Online
DOI: 10.1039/D6TA00999A

performance, suggesting that the use of PET-derived TPA does not adversely affect the intrinsic OER and EGOR kinetics of the Co-MOF (**Figure S13**). This highlights the dual benefit of PET plastic upcycling and efficient electrocatalysis, reinforcing the potential of recycled linkers in advanced energy and chemical conversion applications.

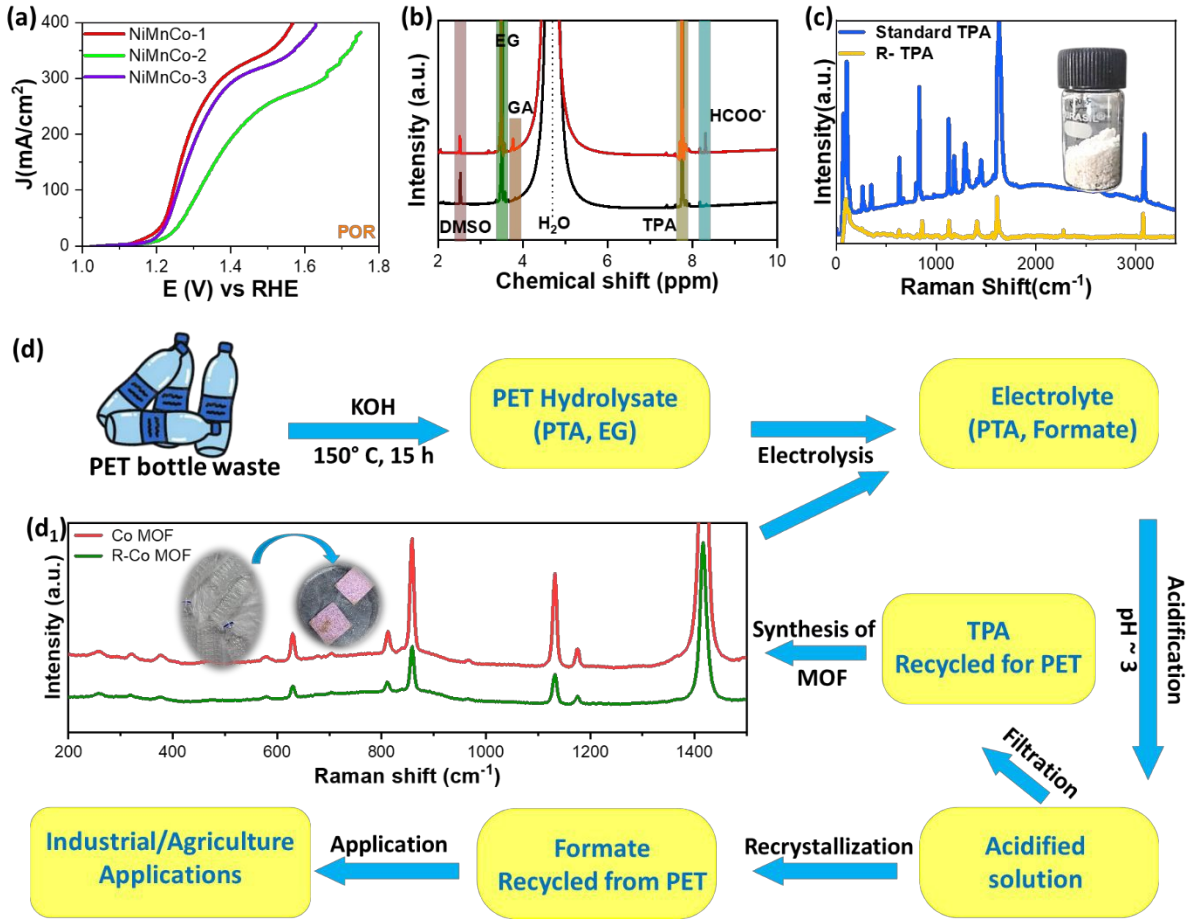

Figure 5 (a) Polarization curves for PET hydrolysate oxidation reaction (POR) (with iR compensation), (b) ^{1}H NMR spectra of PET hydrolysate before and after electrolysis, (c) Raman spectra of standard and recovered TPA, (d) Schematic of electro-upcycling of PET plastic into value added products such as formate and TPA, inset Figure 5-d_1 is the Raman spectra and digital image of Co-MOF synthesized from R-TPA and standard TPA.

Figure S14-a,b shows the long-term chrono-potentiometry curves at current density of 100 mA/cm^2 in alkaline electrolyte with and without 0.3 M EG. During EG electrolysis, the cell voltage remains highly stable over an extended operation period of ~90 hr, exhibiting only a marginal increase with time. Notably, upon periodic replacement with fresh electrolyte, an immediate recovery of the initial cell voltage is observed. The present behaviour suggests that

View Article Online
DOI: 10.1039/D6TA00999A

slow rise in the cell voltage during continuous electrolysis is primarily due to reduction in the EG concentration in electrolyte, rather than from irreversible catalyst degradation. The restoration of performance confirms the structural and chemical robustness of the NiMnCo-MOF electrode under EGOR conditions[56,57]. Even, the electrolysis performance for water electrolysis is stable for operation period of ~70 hr. The post-stability SEM analysis suggests that the catalyst surface retains its flower-like architecture composed of thin, interconnected nanosheets, even after prolonged electrolysis in both OER and EGOR conditions (**Figure S14-c-e**). The structure of NiMnCo-1 was further investigated using powder XRD (**Figure S15**). The powder XRD shows significantly reduced peaks associated with the original MOF-architecture, which is well-supported by in-situ Raman spectroscopy. Conversely, the MOF architecture is well-preserved after the EGOR stability test. This suggests that the reconstruction is controlled, allowing the crystalline structure to remain intact, unlike in OER. The modulation in surface chemical composition and valence states owing to surface re-construction during OER and EGOR was further investigated by XPS analysis. **Figure S16-a** shows the Co 2p spectra of NiMnCo-1 electrocatalysts after OER and EGOR stability test, exhibiting the spin-orbit doublet for Co^{2+} and Co^{3+} electronic states. The Co^{3+}/Co^{2+} ratio is enhanced from 0.63 (before electrolysis) to 0.92 for EGOR and 1.08 for OER, confirms the oxidation of Co^{2+} to Co^{3+} during anodic reactions. Additionally, peaks are slightly shifted to lower binding energy after OER and EGOR performance, attributing to more dynamic anodic performance after surface re-construction. The post-stability Ni 2p spectra confirms increase in the Ni^{3+}/Ni^{2+} ratio from 0.47 (before electrolysis) to 0.73 for EGOR and 0.65 for OER (**Figure S16-b**). These results confirm the formation of NiOOH and CoOOH species in anodic condition, which is in well-agreement with results of in-situ Raman spectroscopy. **Figure S16-c** shows the preservation of multivalent Mn-species in NiMnCo-1 electrodes after OER and EGOR performance. The overall hierarchical morphology remains intact, indicating strong

View Article Online
DOI: 10.1039/D6TA00999A

adhesion to the Ni-foam substrate and resistance against electrochemical corrosion[58]. This well-preserved nanosheet frameworks are beneficial for maintaining high electrochemically active surface area, efficient mass transport, and rapid charge transfer during long-term operation.

Conclusion:

In summary, this research demonstrates a rationally engineered NiMnCo-MOF as a highly efficient and selective electrocatalyst for the electrocatalytic upcycling of PET-derived ethylene glycol (EG) into value-added formate. The incorporation of Ni and Mn into Co-MOF facilitates morphological and electronic structure modulation, yielding thin, loosely inter-woven nanosheet architectures with enhanced electrochemically active surface area and low charge-transfer resistance. In-situ Raman spectroscopy reveals controlled surface reconstruction of NiMnCo-MOF under operating conditions, confirming the formation of catalytically active NiOOH and CoOOH sites, which promote EG oxidation reaction via an indirect alcohol-oxidation pathway. This reconstruction effectively suppresses the competing oxygen evolution reaction (OER), enabling a highly selective EG-to-formate conversion with a Faradaic efficiency of 98% at current density of 100 mA/cm^2. With optimized chemical composition, NiMnCo-MOF exhibited superior EGOR performance, delivering a current density of 100 mA/cm^2 at an anodic potential of 1.25 V vs RHE, reducing the anodic potential by 220 mV as compared to conventional OER, underscoring its energy-efficient nature. The catalyst also exhibits notable durability, maintaining stable performance for 90 hr during PET electrolysis and 80 hr during water electrolysis. Furthermore, the successful reuse of PET-derived terephthalate for MOF synthesis demonstrates the circular and sustainable nature of this approach, offering a viable pathway for integrated plastic valorization and green electrocatalysis.

View Article Online
DOI: 10.1039/D6TA00999A

Acknowledgment:

The authors are thankful to CHARUSAT for providing research facilities and financial support to conduct this research. The authors are thankful to the Department of Science & Technology (DST-PURSE) (SR/PURSE/2023/162(G)) for providing the experimental facility for in-situ Raman spectroscopy and FE-SEM.

Data Availability

Data will be made available on request.

Declaration of Competing Interest:

The authors declare that they have no known competing financial interests or personal relationships that could have appeared to influence the work reported in this paper.

References:

[1] S.K. Kilaparthi, P. Pareek, A. Addad, P. Roussel, S. Szunerits, S. Sampath, R. Boukherroub, Integrated Electrochemical Conversion of Plastic Waste and CO2 to Formate Using Non-Noble-Metal Catalysts: In Situ Raman Study, ACS Appl. Mater. Interfaces. 17 (2025) 50591–50602. https://doi.org/10.1021/acsami.5c08149.

[2] H. Yu, Y. Oh, Y.L. Kim, C. Liu, K. Park, H.G. Cha, M. Delferro, D. Kang, Molecular Level Understanding of Polyethylene Terephthalate (PET) Depolymerization in Base/Alcohol Hybrid Systems, ACS Appl. Mater. Interfaces. 17 (2025) 21097–21109. https://doi.org/10.1021/acsami.4c20887.

[3] H. Wu, H. Tian, L. Chen, W. Luo, S. Li, L. Wang, X. Cui, J. Shi, Advances and Insights in Electrocatalytic Upcycling of Polyethylene Terephthalate Plastic Wastes, Adv. Mater. 38 (2026) e15766. https://doi.org/https://doi.org/10.1002/adma.202515766.

[4] D. Sharma, P. Choudhary, S. Kumar, V. Krishnan, Integrated Chemical Upcycling of Poly(ethylene terephthalate) Waste to Multiple Value-Added Products Catalyzed by Ni2P Supported on SiO2: From Trash-to-Treasure, ACS ES&T Eng. 5 (2025) 2640–2654. https://doi.org/10.1021/acsestengg.5c00357.

[5] V. Kumar, S. Kumar, D. Sharma, V. Krishnan, Nanoarchitectonics of ZnFe-Layered Double Hydroxide Catalysts for Valorization of Waste Polyethylene Terephthalate Bottles into Value-Added Products, Macromol. Rapid Commun. 46 (2025) e00497. https://doi.org/https://doi.org/10.1002/marc.202500497.

[6] W. Li, D. Xiao, X. Gong, X. Xu, F. Ma, Z. Wang, P. Wang, Y. Liu, Y. Dai, Z. Zheng, Y. Fan, B. Huang, Electrocatalytic upgrading of polyethylene terephthalate plastic to formic acid at an industrial-scale current density via Ni-MOF @ MnCo-OH catalyst, Chem. Eng. J. 480 (2024) 148087. https://doi.org/10.1016/j.cej.2023.148087.

[7] F. Ma, Z. Li, R. Hu, Z. Wang, J. Wang, J. Li, Y. Nie, Z. Zheng, X. Jiang, Electrocatalytic Waste-Treating-Waste Strategy for Concurrently Upgrading of Polyethylene Terephthalate Plastic and CO2 into Value-Added Formic Acid, ACS Catal. 13 (2023) 14163–14172. https://doi.org/10.1021/acscatal.3c03428.

[8] P.J. Sharma, S.A. Bhakhar, M.N. Patel, M.N. Nandpal, K.A. Bhakhar, S.G. Patel, P. Sahatiya, G. Nagaraju, C.K. Sumesh, P.M. Pataniya, Binder-free nickel–iron selenide catalyst arrays for coupling hydrogen production with polyethylene terephthalate plastic electro-upcycling, J. Mater. Chem. A. 14 (2026) 1923–1935. https://doi.org/10.1039/D5TA06515A.

[9] M. Du, Y. Zhang, S. Kang, C. Xu, Y. Ma, L. Cai, Y. Zhu, Y. Chai, B. Qiu, Electrochemical Production of Glycolate Fuelled By Polyethylene Terephthalate Plastics with Improved Techno-Economics, Small. 19 (2023) 2303693.

https://doi.org/https://doi.org/10.1002/smll.202303693.

View Article Online
DOI: 10.1039/D6TA00999A

[10] Y. Li, B. Sun, Y. Li, C. Zhang, P.-J. Jin, X. Wang, B.Y. Xia, Y. Chen, X. Ai, Enhancing C–C bond cleavage in ethylene glycol electrooxidation via d–p orbital hybridization at PtBi nanodendrites with ultrathin bimetallene subunits, Adv. Powder Mater. 5 (2026) 100392. https://doi.org/https://doi.org/10.1016/j.apmate.2025.100392.

[11] X.-L. Liu, B. Sun, W. Zhong, Y.-C. Yin, J. Wang, X. Ai, Y. Chen, Ultrathin PdBiRh trimetallene for energy-saving polyethylene terephthalate-derived ethylene glycol electrooxidation coupled carbon dioxide electroreduction, Sci. China Chem. 69 (2026) 503–510. https://doi.org/10.1007/s11426-025-2721-0.

[12] X. Li, J. Sun, H. Ma, X. Long, T. Li, Y. Shimoyama, T. Naito, K. Sato, H. Yamada, K. Nagaoka, Y. Zhao, X. Qian, Efficient metallic Ni as a bifunctional electrocatalyst for integrating continuous PET plastic upcycling with hydrogen production, Appl. Catal. B Environ. Energy. 371 (2025) 125211. https://doi.org/https://doi.org/10.1016/j.apcatb.2025.125211.

[13] P.J. Sharma, K.K. Joshi, S. Siraj, P. Sahatiya, C.K. Sumesh, P. Pataniya, Vanadium-Doped Ni3S2: Morphological Evolution for Enhanced Industrial-Scale Water and Urea Electrolysis, ChemSusChem. n/a (2024) e202401371. https://doi.org/https://doi.org/10.1002/cssc.202401371.

[14] S. Ma, H. Hu, S. Qian, J. Wei, R. Liao, Y. Zhang, H. Zhang, T. Jiang, J. Tian, Tailoring the coordination environment of Co-ZIF-L interpenetrating spindle nanosheets for electrocatalytic upcycling of polyethylene terephthalate plastics, Appl. Catal. B Environ. Energy. 385 (2026) 126279. https://doi.org/https://doi.org/10.1016/j.apcatb.2025.126279.

[15] N. Wang, X. Li, M.-K. Hu, W. Wei, S.-H. Zhou, X.-T. Wu, Q.-L. Zhu, Ordered

macroporous superstructure of bifunctional cobalt phosphide with heteroatomic modification for paired hydrogen production and polyethylene terephthalate plastic recycling, Appl. Catal. B Environ. 316 (2022) 121667. https://doi.org/https://doi.org/10.1016/j.apcatb.2022.121667.

[16] J. Miao, X.-L. Guo, C. Tan, Y.-X. Niu, P. Zhang, P.-J. Zhang, F. Shi, Y. Chen, Hierarchical B and Cu co-doped Co3O4 nanoarrays for nitrate reduction coupled with polyethylene terephthalate plastic upcycling, J. Mater. Chem. A. 13 (2025) 40709–40717. https://doi.org/10.1039/D5TA07327H.

[17] H. Liu, Z. Wang, Y. He, X. Hu, L. Liu, Simultaneous electrochemical upgrading of polyethylene terephthalate plastic and carbon dioxide into valuable chemicals, Appl. Catal. B Environ. Energy. 361 (2025) 124667. https://doi.org/https://doi.org/10.1016/j.apcatb.2024.124667.

[18] K. Wu, C. Cao, K. Li, C. Lyu, J. Cheng, H. Li, P. Hu, J. Wu, W. Lau, X. Zhu, P. Qian, J. Zheng, Regulating electronic structure by Mn doping for nickel cobalt hydroxide nanosheets / carbon nanotube to promote oxygen evolution reaction and oxidation of urea and hydrazine, Chem. Eng. J. 452 (2023) 139527. https://doi.org/10.1016/j.cej.2022.139527.

[19] X. Zhao, C. Kuang, C. An, M. Wang, Preparation of NiCo hydroxide by chloride corrosion for electrocatalytic upcycling of polyethylene terephthalate plastic waste, Chem. Eng. J. 500 (2024) 157275. https://doi.org/https://doi.org/10.1016/j.cej.2024.157275.

[20] Z.-H. Zhang, Z.-R. Yu, Y. Zhang, A. Barras, A. Addad, P. Roussel, L.-C. Tang, S. Szunerits, R. Boukherroub, Seawater corrosive engineering assisted in-situ room temperature synthesis of Ni/Co/Fe trimetallic composition to achieve polyester plastics

upgrading and green hydrogen production, Chem. Eng. J. 498 (2024) 155472. https://doi.org/https://doi.org/10.1016/j.cej.2024.155472.

[21] R. Bhabal, S. Gupta, R. Fernandes, M. Gupta, N. Patel, Bifunctional CoPBO/Co-MOF composite electrocatalyst for energy-efficient hydrogen evolution by urea-assisted water splitting, Int. J. Hydrogen Energy. 116 (2025) 299–311. https://doi.org/10.1016/j.ijhydene.2025.03.100.

[22] P.J. Sharma, S.A. Bhakhar, M.N. Nandpal, K.A. Bhakhar, S.G. Patel, P. Sahatiya, C.K. Sumesh, P.M. Pataniya, Electro-upcycling of PET plastic coupled with hydrogen production using the NiCe@NiTe electrocatalyst, J. Mater. Chem. A. 14 (2026) 3591–3604. https://doi.org/10.1039/D5TA08195E.

[23] S. AlAreeqi, C. Ganley, D. Bahamon, K. Polychronopoulou, P. Clancy, L.F. Vega, Rational design of optimal bimetallic and trimetallic nickel-based single-atom alloys for bio-oil upgrading to hydrogen, Nat. Commun. 16 (2025) 2639. https://doi.org/10.1038/s41467-025-57949-6.

[24] W. Li, H. Wang, X. Zheng, L. Ricardez-Sandoval, Q. Wu, G. Bai, A bimetallic strategy to tailoring the surface formation energy and d-band center of Ni-based catalyst for efficient and stable catalytic hydrogenation of dioctyl phthalate, Chem. Eng. J. 453 (2023) 139779. https://doi.org/https://doi.org/10.1016/j.cej.2022.139779.

[25] W. Xu, X. Chen, J. Chen, H. Jia, Bimetal oxide CuO/Co3O4 derived from Cu ions partly-substituted framework of ZIF-67 for toluene catalytic oxidation, J. Hazard. Mater. 403 (2021) 123869. https://doi.org/10.1016/j.jhazmat.2020.123869.

[26] S. Nangan, Y. Ding, A.Z. Alhakemy, Y. Liu, Z. Wen, Hybrid alkali-acid urea-nitrate fuel cell for degrading nitrogen-rich wastewater, Appl. Catal. B Environ. 286 (2021). https://doi.org/10.1016/j.apcatb.2021.119892.

[27] Y. Zhai, L. Cai, Z. Gong, W. Hu, Z. Li, Molybdenum-doped Co3S4 nanoarrays as outstanding catalysts for overall water splitting, CrystEngComm. 26 (2024) 995–1003. https://doi.org/10.1039/D3CE01132A.

[28] S. De, B.P. Bastakoti, Bimetallic (Co/Ni, Ce) MOF decorated V2CTx MXene/CNT for high energy flexible zinc-ion capacitor, J. Mater. Chem. A. (2026). https://doi.org/10.1039/D5TA08281A.

[29] V. Saranya, S.M. Mariappan, M. Navaneethan, J. Archana, Modulating spin states in dual active sites of CoFe electrocatalysts for energy harvesting applications, J. Mater. Chem. A. (2026). https://doi.org/10.1039/D5TA07535A.

[30] Q. Qi, C. Zhang, J. Hu, Triggered factors and structure-activity relationship in the dynamic reconstruction processing of MOF for the alkaline oxygen evolution reaction, Coord. Chem. Rev. 522 (2025) 216235. https://doi.org/https://doi.org/10.1016/j.ccr.2024.216235.

[31] Z. Shi, Z. Yu, R. Jiang, J. Huang, Y. Hou, J. Chen, Y. Zhang, H. Zhu, B. Wang, H. Pang, MOF-derived M-OOH with rich oxygen defects by in situ electro-oxidation reconstitution for a highly efficient oxygen evolution reaction, J. Mater. Chem. A. 9 (2021) 11415–11426. https://doi.org/10.1039/D1TA01638E.

[32] S. Hernández-Salvador, I. Márquez, S. Gutiérrez-Tarriño, J.J. Calvente, J.L. del Río-Rodríguez, P. Oña-Burgos, R. Andreu, J.L. Olloqui-Sariego, Selective design of MOF-derived electrocatalytic interphases by potential-driven surface reconstruction, Electrochim. Acta. 525 (2025) 146158. https://doi.org/https://doi.org/10.1016/j.electacta.2025.146158.

[33] M. Zhong, T. Chen, J. Wang, J. Yuan, W. Ju, Electrochemical Reconstruction of CoxNi1-x-MOF-74 Microfibers: Influence of Atomic Ratio on Morphological

View Article Online
DOI: 10.1039/D6TA00999A

Evolution, J. Phys. Chem. C. 129 (2025) 6850–6860. https://doi.org/10.1021/acs.jpcc.5c00537.

[34] Z.-L. Huang, M. Drillon, N. Masciocchi, A. Sironi, J.-T. Zhao, P. Rabu, P. Panissod, Ab-Initio XRPD Crystal Structure and Giant Hysteretic Effect (Hc = 5.9 T) of a New Hybrid Terephthalate-Based Cobalt(II) Magnet, Chem. Mater. 12 (2000) 2805–2812. https://doi.org/10.1021/cm000386c.

[35] Q. Wang, H. Xu, X. Qian, G. He, H. Chen, Sulfur vacancies engineered self-supported Co3S4 nanoflowers as an efficient bifunctional catalyst for electrochemical water splitting, Appl. Catal. B Environ. 322 (2023). https://doi.org/10.1016/j.apcatb.2022.122104.

[36] K.I. Hadjiivanov, D.A. Panayotov, M.Y. Mihaylov, E.Z. Ivanova, K.K. Chakarova, S.M. Andonova, N.L. Drenchev, Power of Infrared and Raman Spectroscopies to Characterize Metal-Organic Frameworks and Investigate Their Interaction with Guest Molecules, Chem. Rev. 121 (2021) 1286–1424. https://doi.org/10.1021/acs.chemrev.0c00487.

[37] J. Zhang, H. Ni, J. Yu, B. Zhao, Ni-Doped Co-Based Metal–Organic Framework with Its Derived Material as an Efficient Electrocatalyst for Overall Water Splitting, Catalysts. 15 (2025). https://doi.org/10.3390/catal15040355.

[38] Y. Wang, S. Guo, X. Xin, Y. Zhang, B. Wang, S. Tang, X. Li, Effective interface contact on the hierarchical 1D/2D CoO/NiCo-LDH heterojunction for boosting photocatalytic hydrogen evolution, Appl. Surf. Sci. 549 (2021) 149108. https://doi.org/https://doi.org/10.1016/j.apsusc.2021.149108.

[39] A. Vinu, D.P. Sawant, K. Ariga, M. Hartmann, S.B. Halligudi, Benzylation of benzene and other aromatics by benzyl chloride over mesoporous AlSBA-15 catalysts,

View Article Online
DOI: 10.1039/D6TA00999A

Microporous Mesoporous Mater. 80 (2005) 195–203. https://doi.org/https://doi.org/10.1016/j.micromeso.2004.12.012.

[40] P.J. Sharma, N.M. Solanki, K.H. Modi, U. Purohit, S. Siraj, P. Sahatiya, S.K. Gupta, P.N. Gajjar, C.K. Sumesh, P.M. Pataniya, Enhanced water and urea electrolysis at industrial scale current density using self-supported VxNi1-xO trifunctional catalysts, Int. J. Hydrogen Energy. 85 (2024) 374–384. https://doi.org/10.1016/j.ijhydene.2024.08.352.

[41] P.M. Pataniya, P.J. Sharma, S.A. Bhakhar, N. Rajani, M.N. Nandpal, K.A. Bhakhar, S.G. Patel, C. Vijayakumar, S. CK, Coupling Polyethylene Terephthalate Plastic Upcycling and Hydrogen Evolution Using Cerium-Doped Nickel Cobalt Sulfide Electrocatalysts, ACS Appl. Mater. Interfaces. 18 (2026) 1843–1853. https://doi.org/10.1021/acsami.5c22894.

[42] V. Singh, D.K. Singh, M. Yadav, S. Singh, V. Rathour, A. Tiwari, V. Ganesan, A Co and Fe bimetallic MOF with enhanced electrocatalytic oxygen evolution performance: exploring the electronic environment modifications upon Fe incorporation, Energy Adv. 3 (2024) 636–647. https://doi.org/10.1039/D3YA00572K.

[43] Z. Yu, Y. Li, V. Martin-Diaconescu, L. Simonelli, J. Ruiz Esquius, I. Amorim, A. Araujo, L. Meng, J.L. Faria, L. Liu, Highly Efficient and Stable Saline Water Electrolysis Enabled by Self-Supported Nickel-Iron Phosphosulfide Nanotubes With Heterointerfaces and Under-Coordinated Metal Active Sites, Adv. Funct. Mater. 32 (2022) 2206138. https://doi.org/https://doi.org/10.1002/adfm.202206138.

[44] A.M. Shah, K.H. Modi, P.M. Pataniya, K.S. Joseph, S. Dabhi, G.R. Bhadu, C.K. Sumesh, Self-Supported Mn-Ni3Se2 Electrocatalysts for Water and Urea Electrolysis for Energy-Saving Hydrogen Production, ACS Appl. Mater. Interfaces. 16 (2024)

11440–11452. https://doi.org/10.1021/acsami.3c16244.

View Article Online
DOI: 10.1039/D6TA00999A

[45] D. Han, Z. Song, B. Liu, X. Zhang, J. Liu, Y. Huang, C. Xing, J. Zhang, Mn doping induces oxygen-rich vacancies to regulate Co2+ cyclic regeneration and synergistically promote PMS activation and pollutant degradation, J. Mol. Struct. 1349 (2026) 143895. https://doi.org/https://doi.org/10.1016/j.molstruc.2025.143895.

[46] Y. Ji, W. Cheng, C. Li, X. Liu, Oxygen Vacancies of CeO2 Nanospheres by Mn-Doping: An Efficient Electrocatalyst for N2 Reduction under Ambient Conditions, Inorg. Chem. 61 (2022) 28–31. https://doi.org/10.1021/acs.inorgchem.1c02989.

[47] T. Kim, S. Kim, H. Jeong, Y. Im, N. Park, M. Kang, Improved OH adsorption and effective oxygen evolution reaction on carbon-capsulated Co0.1Ni0.9O@C/CP electrode, Appl. Surf. Sci. 655 (2024) 159549. https://doi.org/https://doi.org/10.1016/j.apsusc.2024.159549.

[48] X. Lin, Q. Li, Y. Hu, Z. Jin, K.M. Reddy, K. Li, X. Lin, L. Ci, H.J. Qiu, Revealing Atomic Configuration and Synergistic Interaction of Single-Atom-Based Zn-Co-Fe Trimetallic Sites for Enhancing Oxygen Reduction and Evolution Reactions, Small. 2300612 (2023) 1–9. https://doi.org/10.1002/smll.202300612.

[49] D. Xiong, X. He, Z. Zhu, T. Liu, D. Wu, Y. Zou, Z. Chen, Upcycling Polybutylene Succinate Waste to Succinic Acid via Paired Electrocatalytic using Thiol-Engineered MOFs and a CO2-Assisted Precipitation System, Adv. Funct. Mater. 36 (2026) e18434. https://doi.org/https://doi.org/10.1002/adfm.202518434.

[50] S. Cersoy, V. Rouchon, O. Belhadj, J. Cuisin, M. Herbin, Noninvasive Fluid Identification: Potential of Micro-Raman Spectroscopy, Collect. Forum. 34 (2021) 53–72. https://doi.org/10.14351/0831-4985-34.1.53.

[51] S.O. Liubimovskii, V.S. Novikov, L.Y. Ustynyuk, P. V Ivchenko, K.A. Prokhorov, V V Kuzmin, E.A. Sagitova, M.M. Godyaeva, S. V Gudkov, M.E. Darvin, Spectrochimica Acta Part A : Molecular and Biomolecular Spectroscopy Raman structural study of ethylene glycol and 1 , 3-propylene glycol aqueous solutions, Spectrochim. Acta Part A Mol. Biomol. Spectrosc. 285 (2023) 121927. https://doi.org/10.1016/j.saa.2022.121927.

[52] G. Wu, X. Dong, J. Mao, G. Li, C. Zhu, S. Li, Anodic glycerol oxidation to formate facilitating cathodic hydrogen evolution with earth-abundant metal oxide catalysts, Chem. Eng. J. 468 (2023) 143640. https://doi.org/10.1016/j.cej.2023.143640.

[53] Z. He, J. Hwang, Z. Gong, M. Zhou, N. Zhang, X. Kang, J.W. Han, Y. Chen, Promoting biomass electrooxidation via modulating proton and oxygen anion deintercalation in hydroxide, Nat. Commun. 13 (2022) 3777. https://doi.org/10.1038/s41467-022-31484-0.

[54] M. Rafiee, D.J. Abrams, L. Cardinale, Z. Goss, A. Romero-Arenas, S.S. Stahl, Cyclic voltammetry and chronoamperometry: mechanistic tools for organic electrosynthesis, Chem. Soc. Rev. 53 (2024) 566–585. https://doi.org/10.1039/d2cs00706a.

[55] X. Ma, L. Schröck, G. Gao, Q. Ai, M. Zarrabeitia, C. Liang, M.Z. Hussain, R. Khare, K.T. Song, D.J. Zheng, M. Koch, I.E.L. Stephens, S. Hou, Y. Shao-Horn, J. Warnan, A.S. Bandarenka, R.A. Fischer, Tuning the Reconstruction of Metal-Organic Frameworks during the Oxygen Evolution Reaction, ACS Catal. 14 (2024) 15916–15926. https://doi.org/10.1021/acscatal.4c03618.

[56] P.J. Sharma, K.K. Joshi, P. Sahatiya, C.K. Sumesh, P.M. Pataniya, Functional nickel iron sulphide/hydroxide catalysts for hydrazine oxidation and energy saving hydrogen production, J. Mater. Chem. A. 13 (2025) 9865–9877.

https://doi.org/10.1039/D4TA08796H.

View Article Online
DOI: 10.1039/D6TA00999A

[57] P.J. Sharma, K.K. Joshi, S. Siraj, P. Sahatiya, C.K. Sumesh, P. Pataniya, Vanadium-Doped Ni3S2: Morphological Evolution for Enhanced Industrial-Scale Water and Urea Electrolysis, ChemSusChem. 18 (2025) e202401371. https://doi.org/10.1002/cssc.202401371.

[58] A. Kumar, S. Bhattacharyya, Porous NiFe-Oxide Nanocubes as Bifunctional Electrocatalysts for Efficient Water-Splitting, ACS Appl. Mater. Interfaces. 9 (2017) 41906–41915. https://doi.org/10.1021/acsami.7b14096.

View Article Online
DOI: 10.1039/D6TA00999A

View Article Online
DOI: 10.1039/D6TA00999A

Data Availability:

Data will be made available on request.